

Estimation of woodland canopy structure with terrestrial LiDAR: expanded methods

John L. Godlee

Contents

1	Introduction	2
2	Sampling	2
3	Field measurements	4
3.1	Trees	4
3.2	Grass biomass	5
3.3	Hemispherical photography	6
3.4	Stand structure	7
4	Terrestrial LiDAR	11
4.1	Voxelisation	13
4.2	Noise reduction	13
4.3	LiDAR analysis	15
4.3.1	Foliage density profiles	15
4.3.2	Canopy cover	18
4.3.3	Grass biomass estimation	20
4.3.4	Canopy rugosity	21
5	Statistical analysis	23
5.1	Foliage density profiles	23
5.2	Grass biomass	23
5.3	Canopy rugosity	24

1 1 Introduction

2 This document provides detailed field and analytical methods for the study of tree canopy struc-
3 ture in southern African woodlands. The study aimed to understand the effects of tree species di-
4 versity and stand structure on tree canopy structure and grass biomass. Chapter XXX contains
5 the same methods in brief.

6 2 Sampling

7 Fieldwork was conducted at two sites, the first in Bicuar National Park, southwest Angola ($S15.1^\circ$,
8 $E14.8^\circ$), and the second in and around Mtarure Forest Reserve, southeast Tanzania ($S9.0^\circ$, $E39.0^\circ$).
9 Fieldwork was conducted during the peak growth period of each site, in order to capture the high-
10 est foliage volume in the canopy and grass volume in the understorey.

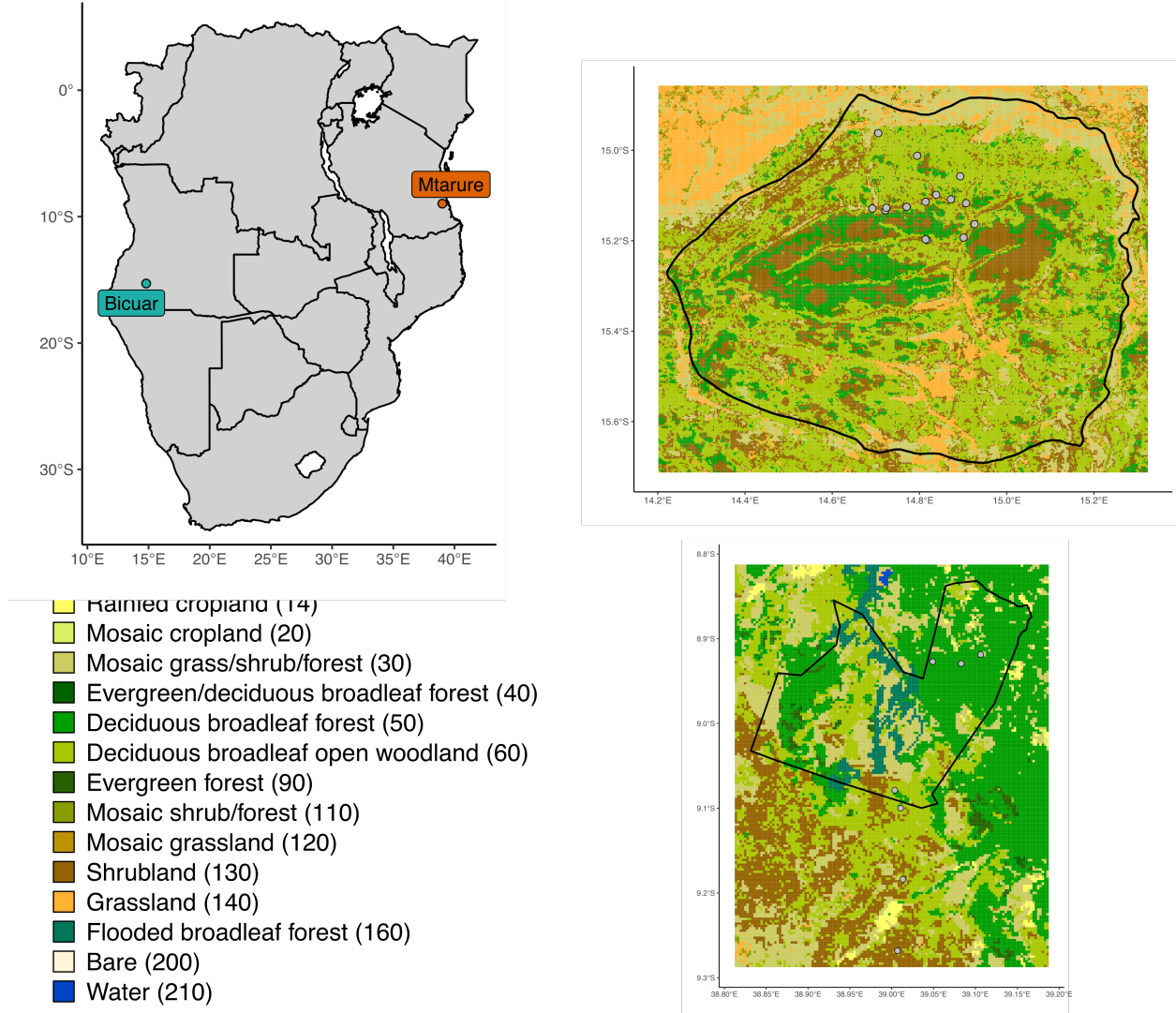


Figure 1: Location of study sites within southern Africa (a), and of 1 ha plots within each site. The black polygons denote the boundaries of protected areas which encompass the majority of study sites, Bicuar National Park in Angola (b), and Mtarure Forest Reserve in Tanzania (c). Each site map is coloured according to the GlobCover global land cover classification.

Site	MAT (°C)	MAP (mm y ⁻¹)	Temp. range (°C)	CWD
				(mm y ⁻¹)
Bicuar	20.8 (0.70)	825.9 (52.01)	24.5 (0.90)	-844.8 (44.29)
Mtarure	25.7 (0.24)	958.4 (25.19)	12.0 (0.33)	-739.6 (8.06)

Table 1: Climatic data for each site, extracted from WorldClim at 2.5 minute resolution. Values are the mean and standard deviation (in brackets) of all pixels intersecting each protected area.

11 At each site, a number of 1 ha permanent plots were sampled. In Angola, 15 plots were sampled,
12 while in Tanzania, only seven were sampled, following the curtailment of fieldwork due to COVID-

13 19 travel restrictions. Permanent plots were located in areas of homogeneous vegetation type,
 14 away from roads and undisturbed by humans. Plots were established following the SEOSAW pro-
 15 tocol (version 3.0, SEOSAW 2020). Plots were located quasi-randomly by first locating areas from
 16 satellite imagery expected to comprise savanna woodland vegetation. At each site, plots were de-
 17 liberately located along a gradient of stem density.
 18 Each permanent plot was further subdivided into nine 10 m diameter circular subplots arranged in
 19 a regular grid, with a buffer from the plot edge (Figure 2).

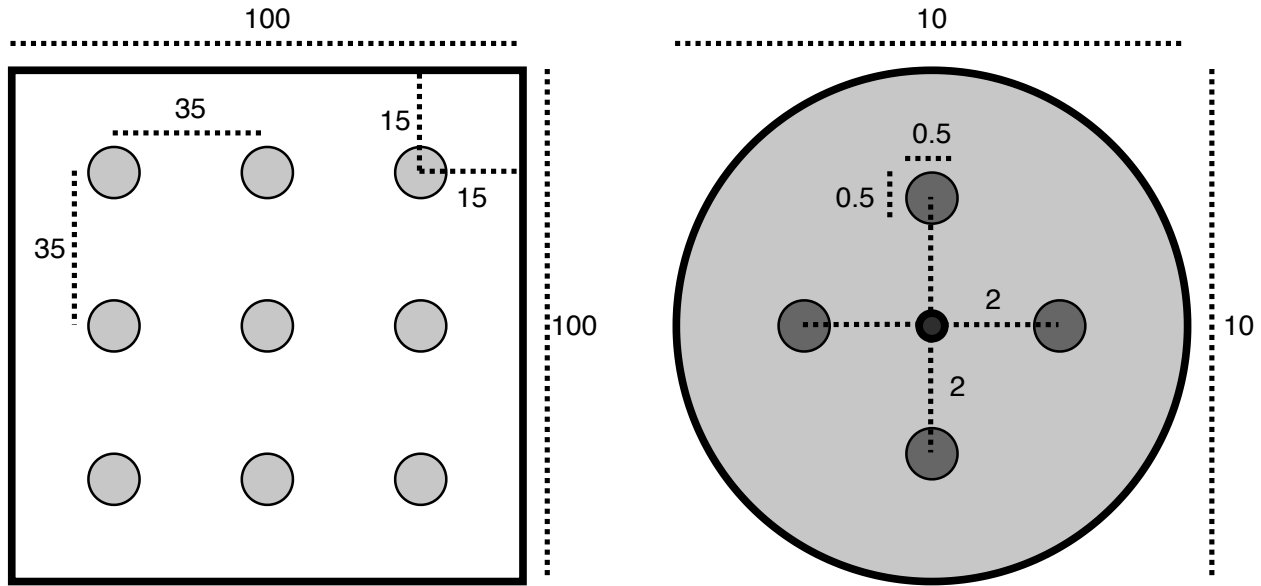


Figure 2: The layout of 10 m diameter subplots within each 1 ha square plot. Each subplot is situated inside a 15 m buffer from the plot edge, with 35 m between subplot centres. Subplots are arranged in a 3x3 grid. Disc-pasture measurements and biomass samples are located in cardinal directions 2 m from the centre of the subplot. All distances are in metres.

20 3 Field measurements

21 3.1 Trees

22 For each subplot, we measured all woody stems >5 cm stem diameter with canopy material inside
 23 the subplot. For each stem we recorded:

- 24 • Tree identity
- 25 • Stem diameter (diameter at breast height - 1.3 m)

26 For each tree, which may be composed of multiple stems joined at the base, we recorded:

- 27 • Species

- 28 • Height to top of canopy
- 29 • Canopy area, ellipse from two perpendicular measurements (Figure 3)
- 30 • Distance from subplot centre
- 31 • Compass direction from subplot centre

Plot edges

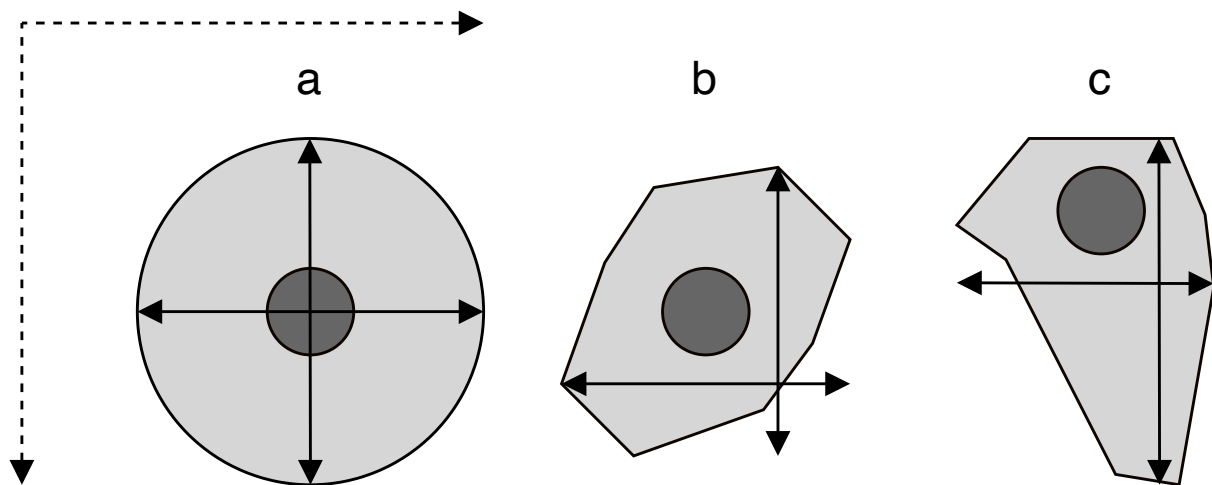


Figure 3: Examples of tree crowns as viewed from above to demonstrate how crown extent measurements are located. Darker grey circles show the main stem while pale grey polygons show the maximum extent of the crown. Extent measurements are taken parallel to the plot edges. a) shows a perfectly circular tree crown, b) and c) show irregular tree crowns, demonstrating that maximum crown extent in a given orientation be offset from the stem.

3.2 Grass biomass

32 Grass volume and biomass within each subplot was estimated from four sample points located 2
 33 m from the subplot centre in cardinal directions (Figure 2). At each point, a disc-pasture meter
 34 measurement was taken with a 45.8 cm radius disc weighing exactly 1.5 kg (Bransby and Tain-
 35 ton, 1977). Small woody stems were removed from disc-pasture sample points before the disc-
 36 pasture measurement was taken. The location of the sample point was moved if the designated
 37 point intersected with coarse woody debris, rocks, shrubs, or standing trees. Within each 1 ha
 38 plot, biomass harvesting was conducted at nine randomly allocated disc-pasture sample points.
 39 Tree leaf litter was removed from biomass samples. Biomass harvesting involved clipping all grass
 40 material within the 45.8 cm radius to ground level, taking care not to include roots. Grass sam-
 41 ples from Angola were dried until the mass remained constant (± 5 g) for >48 hours, then weighed
 42

43 to ascertain the grass biomass. Grass samples from Tanzania could not be processed due to cur-
44 tailment of fieldwork due to COVID-19 travel restrictions.

45 **3.3 Hemispherical photography**

46 At the centre of each subplot a single photograph was taken with a Nikon D750 full-frame DSLR
47 camera, with a circular fisheye lens. The lens had an equisolid (equal area) projection, which avoids
48 image distortion. The projection function is given by:

$$R = 2f \sin(\theta/2) \quad (1)$$

49 Where R is the radial position of a point on the image on the sensor, f is the focal length of the
50 lens, and θ is the angle in radians of the desired angular radius of the cropped image.

51 The photo was taken facing directly to zenith, with the top of the camera facing magnetic north,
52 at a height of 1.3 m or above understorey vegetation, whichever was higher. Table 2 shows de-
53 scribes the camera settings for each hemispherical photo.

Table 2: Description of camera settings used for each hemispherical photo. Note that the values of shutter speed and ISO are deliberately variable within sensible thresholds to adapt to light conditions.

Setting	Value
Camera model	Nikon D750
Lens model	Sigma 8 mm f/3.5 EX DG Circular Fisheye
Pixel pitch	5.95 µm
Sensor resolution	24.3 MP
Shutter speed	>1/60s
Aperture	5-7
ISO	100-200
Exposure compensation	-0.7 (Brusa and Bunker, 2014)
Focus	∞ (Hu and Zhu, 2009; Frazer et al., 2001)
Image size	Large Fine JPEG - circular image 4016x4016 px
Orientation	Landscape

54 Photos were captured under uniform light conditions as much as possible, either under overcast

55 skies or early in the day before direct sunlight could be seen on the photo.
 56 ImageJ (Fiji version 2.1.0/1.53c) was used to binarize hemispherical photos (), to separate plant
 57 material from sky. We first split each image into red, green and blue channels. We used the Huang
 58 algorithm to automatically threshold images, using the blue channel only, under the assump-
 59 tion that plant material reflects little blue light, while the sky reflects much more (). Images were
 60 saved as PNG at the original pixel resolution.

61 **3.4 Stand structure**

62 From the stem measurements we calculated a number of indices to characterise whole-plot and
 63 subplot stand structure.

64 We calculated the mean of the spatial mingling index (M_i) according to von Gadow and Hui (2002)
 65 at the plot level, with the adjustment for potential neighbourhood species pool suggested by Hui,
 66 Zhao, et al. (2011). The spatial mingling index is a spatially explicit estimate of the degree to
 67 which species are spatially mixed within a plot:

$$M = \overline{M_i} \quad (2)$$

$$M_i = \frac{S_i}{n_{\max}} \frac{1}{k} \sum_{j=1}^k v_j \quad (3)$$

$$\text{with } v_j = \begin{cases} 0, & \text{neighbour } j \text{ same species as reference } i \\ 1, & \text{otherwise} \end{cases} \quad (4)$$

$$(5)$$

68 where k is the number of nearest neighbours considered for each reference tree, S_i is the number
 69 of species found among the k nearest neighbours of tree i , n_{\max} is the potential number of species
 70 in the neighbourhood, i.e. $k + 1$, and N is the total number of trees in the plot. In our case we
 71 used the conventional value of $k = 4$ (von Gadow and Hui, 2002; Hui and Albert, 2004; Hui, von
 72 Gadow, et al., 2007). The value of M_i increases with greater mixing of species, and all else being
 73 equal will increase with number of species within the plot (Figure 4).

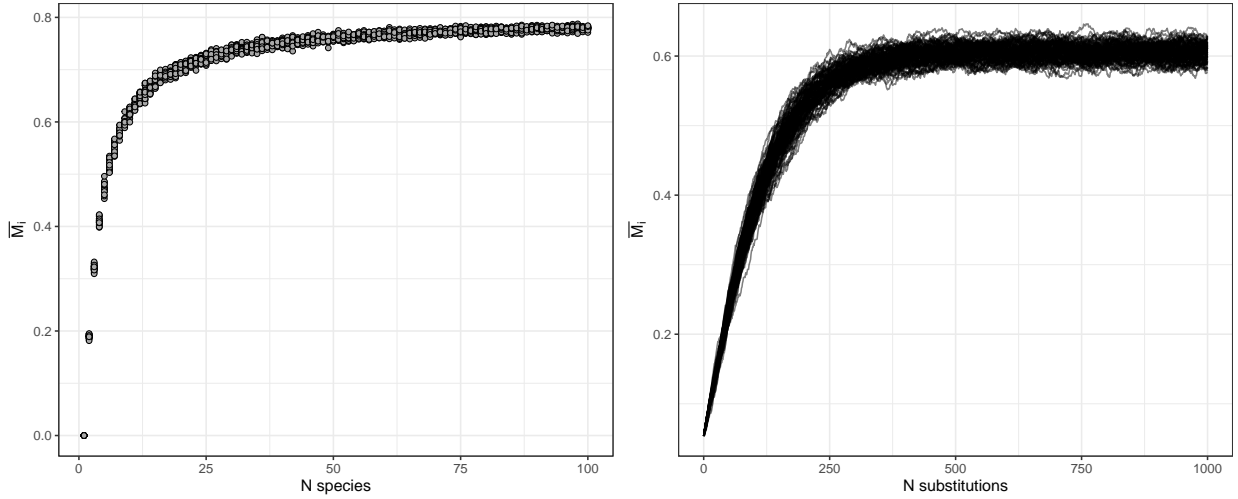


Figure 4: The behaviour of M_i with increasing number of species (left), and increasing spatial mixing of species. The left panel was generated by randomly assigning different numbers of species, in equal proportions, to an evenly spaced grid of individuals. 20 replicates were conducted for each number of species. The right panel was generated by randomly swapping pairs of individuals in a plot with 9 species arranged in mono-specific square blocks in an evenly spaced grid. Each line shows a single replicate, where individuals were swapped in an additive fashion, with 100 total.

74 We also calculated the mean of the winkelmass W_i according to von Gadow and Hui (2002) at the
 75 plot level. The winkelmass estimates the degree of spatial uniformity in stem spatial distribution:

$$W = \overline{W_i} \quad (6)$$

$$W_i = \frac{1}{k} \sum_{j=1}^k v_j \quad (7)$$

$$\text{with } v_j = \begin{cases} 0, & \alpha_j \leq \alpha_0 \\ 1, & \text{otherwise} \end{cases} \quad (8)$$

$$(9)$$

76 where α_j is the angle between consecutive neighbours and α_0 is the critical angle, where $\alpha_0 =$
 77 $360/k$. The value of the winkelmass increases with increasing spatial clumping (decreasing spatial
 78 regularity) of individuals (Figure 6), and in a plot with random tree distribution will increase as
 79 more neighbours are considered (Figure 7).

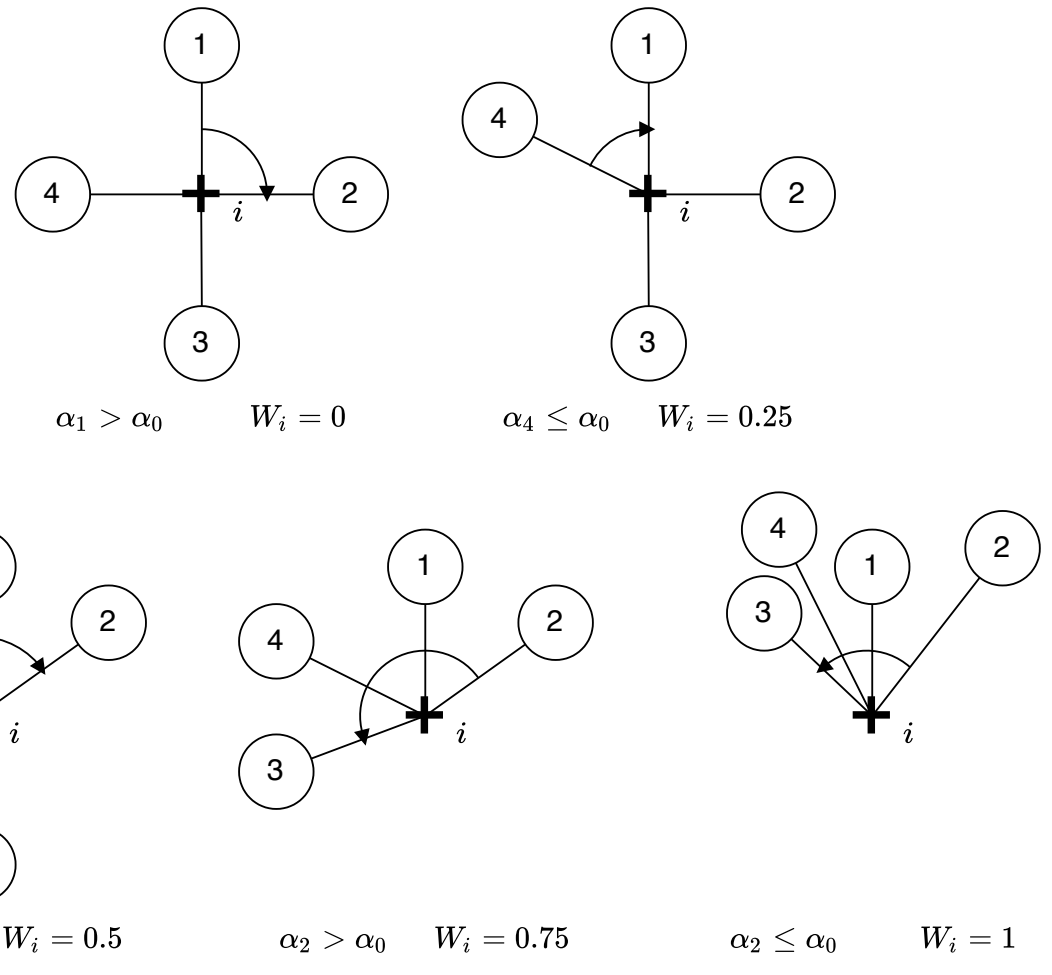


Figure 5: Possible values of W_i at a sample point i , denoted by a cross. Neighbours are represented as circles numbered sequentially from 1 to 4, where $k = 4$. The angles of arrows in each example are given below, along with the winkelmass for that example.

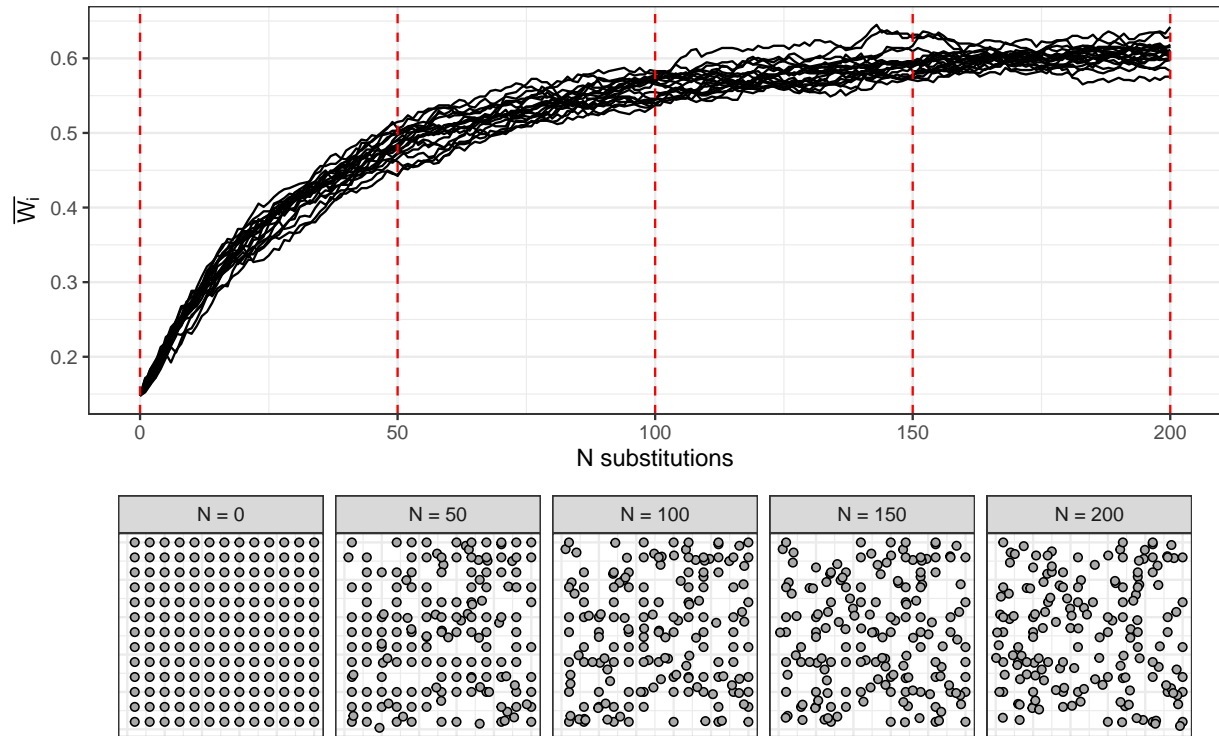


Figure 6: Variation in winkelmass with increasing spatial irregularity of individuals. The top panel shows variation of winkelmass in 20 plots as individuals are sequentially moved to a random location within the plot. Red dotted lines correspond to the panels below which show the spatial distribution of individuals after a given number of random individual movements.

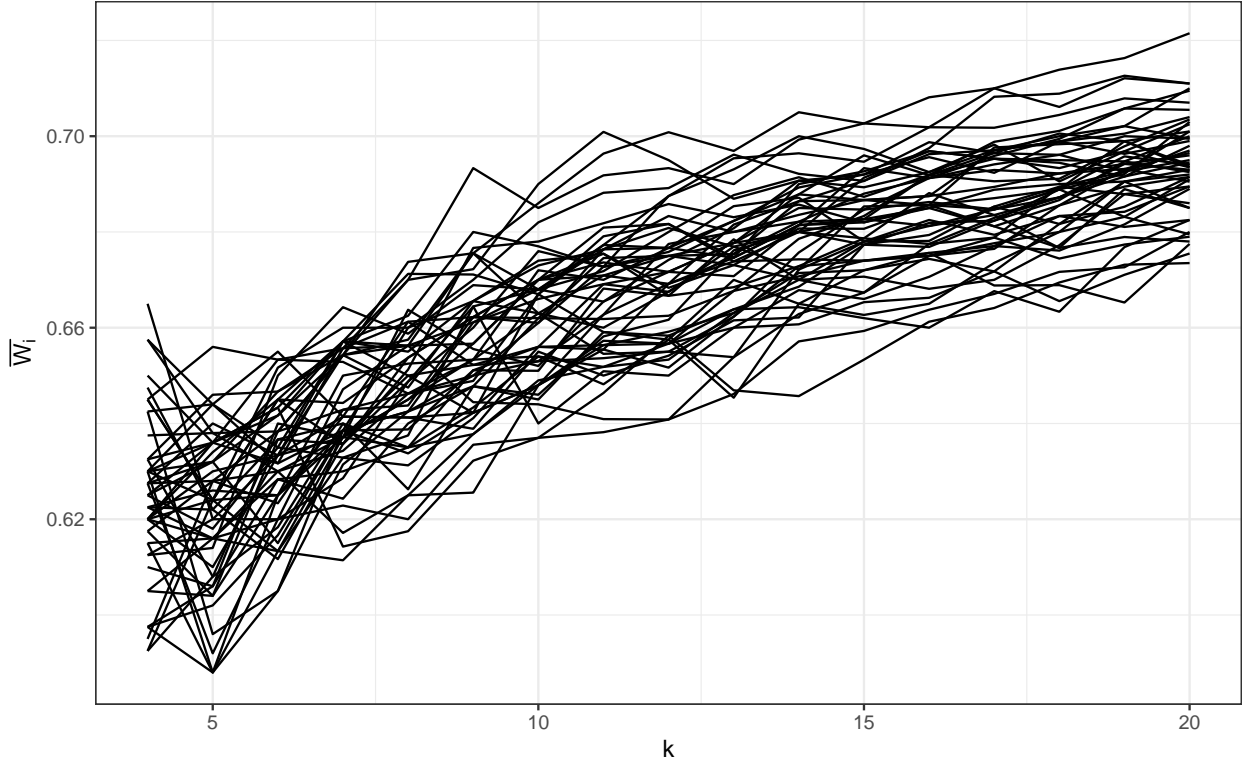


Figure 7: Variation in winkelmass with increasing number of neighbours k considered in the calculation. 50 replicate plots were used, each with 100 individuals randomly distributed in space.

80 To estimate tree spatial structure in subplots we used an adapted version of the Iterative Hegyi
 81 index (H_i) (Hegyi, 1974). Our adapted formula allows the index to be based on a point rather
 82 than a focal tree, transforming it from a tree-centric competition index to a point-centric crowding
 83 index:

$$H_i = \log \sum_{j=1}^n \left(\frac{1}{L_{ij}} D_j \right) \quad (10)$$

84 where D_j is the stem diameter of neighbour tree j and L_j is the distance of the neighbour from
 85 the subplot centre.

86 4 Terrestrial LIDAR

87 Within each subplot, a variable number of scans were recorded using a Leica HDS6100 phase-
 88 shift terrestrial laser scanner (TLS). The number and position of scans within a subplot was de-
 89 termined by the arrangement and density of canopy material in the subplot. Scan positions were
 90 arranged to minimise shadows within the canopy, and to maximise canopy penetration. Number of
 91 scans per subplot ranged between one and five in both Angola and Tanzania (Table 3).

92 Five Leica 6" planar tilt and turn cross-pattern reflective targets were used at each subplot to
 93 align scans. To allow registration of scans among subplots, the location of each target was regis-
 94 tered using a Leica VIVA GS10 GNSS unit, set up in post-processed kinematic (PPK) configura-
 95 tion with a base-station located \sim 100 m from the edge of each 1 ha plot. The location of each tar-
 96 get was measured for at least 4 minutes. Further, we used the TrimbleRTX GNSS post-processing
 97 service to precisely locate each target (Chen et al., 2011). When registering scans we discarded
 98 targets with location accuracy of >3 cm. Scan registration for each subplot was conducted in Le-
 99 ica Cyclone (version 9.1). After registration, scan scenes were exported from Cyclone as PTX files,
 100 one per subplot.

Table 3: Description of scan settings used for each scan.

Setting	Value
Scanner model	Leica HDS6100
Wavelength	650-690 nm
Spot size at exit	3 mm
Beam divergence	0.22 mrad
Range	79 m @90%; 50 m @18% albedo
Azimuth range	0-360°
Zenith range	0-155°
Increments	0.018°
Point spacing over 25 m	7.9 mm
Pixels per line	20000
Lines	10000
Compressed file size	\sim 800 MB
Duration of scan	6 minutes 44 seconds

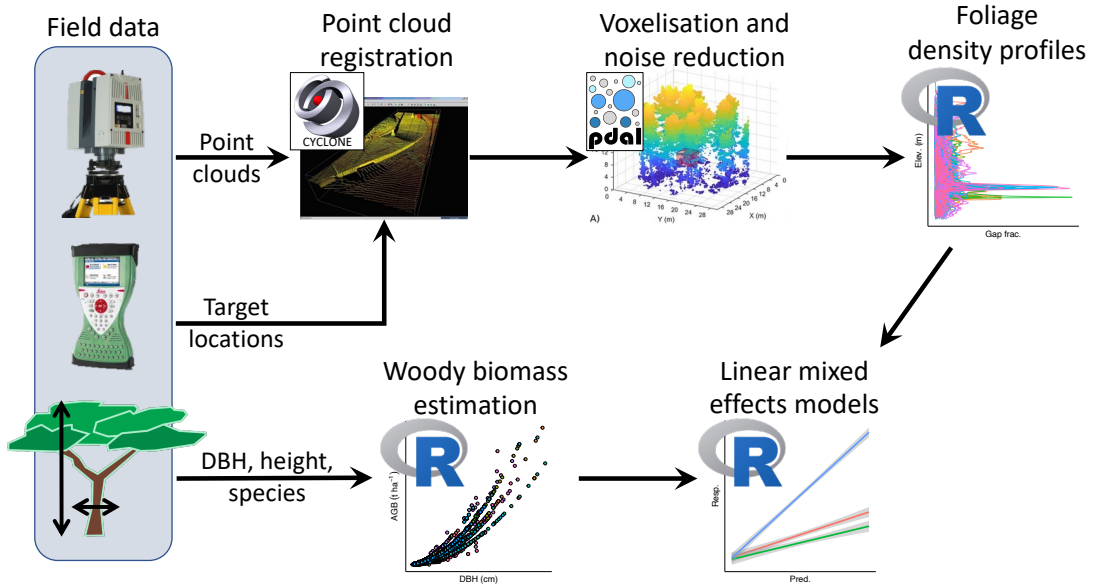


Figure 8: Schematic diagram summarising the data processing and analysis workflow for the TLS data. Processing steps are labelled according to the principal software used during that step.

101 4.1 Voxellation

102 PTX files were converted to compressed LAZ files using PDAL (). The exact code used to ex-
 103 tract and apply the PTX rotation matrix to each point in the PTX file can be found IN THIS
 104 APPENDIX HERE.

105 LAZ files were voxelised to different voxel sizes depending on the application of the data. For
 106 grass biomass estimation, we used 2 cm^3 cubic voxels, while for subplot height profile estimation
 107 we used 5 cm^3 voxels, and for whole plot canopy rugosity we used 10 cm^3 voxels. Variation in
 108 voxel size reflects the spatial scale of each analysis, and is bounded by the beam divergence of the
 109 scanner over longer distances (). Choosing voxels that are too small can result in pock-marked
 110 representations of surfaces that are especially problematic when calculating larger scale canopy
 111 structure metrics, such as canopy top roughness, while voxels that are too large can result in an
 112 over-estimation of plant volume when estimating canopy foliage density at the subplot scale (Sei-
 113 del, Fleck, and Leuschner, 2012; Cifuentes et al., 2014).

114 4.2 Noise reduction

115 Outlier detection and noise reduction was conducted in PDAL using the `filters.outlier` filter,
 116 using the “statistical method” (sensu Rusu et al. 2008), with $k = 8$ (mean number of neighbours),

117 and $m = 1.96$ (standard deviation threshold, approximating a 95% confidence interval):

$$\bar{\mu} = \frac{1}{N} \sum_{i=1}^N \mu_i \quad (11)$$

$$\sigma = \sqrt{\frac{1}{N-1} \sum_{i=1}^N (\mu_i - \bar{\mu})^2} \quad (12)$$

$$t = \mu + m\sigma \quad (13)$$

$$\text{outlier}_i = \begin{cases} \text{true}, & \text{if } \mu_i >= t \\ \text{false}, & \text{otherwise} \end{cases} \quad (14)$$

118 where N is the number of points in the scene, $\bar{\mu}$ is the mean distance to nearest neighbour points,
119 and σ is the standard deviation of these distances. t is the threshold distance used to define an
120 outlier.

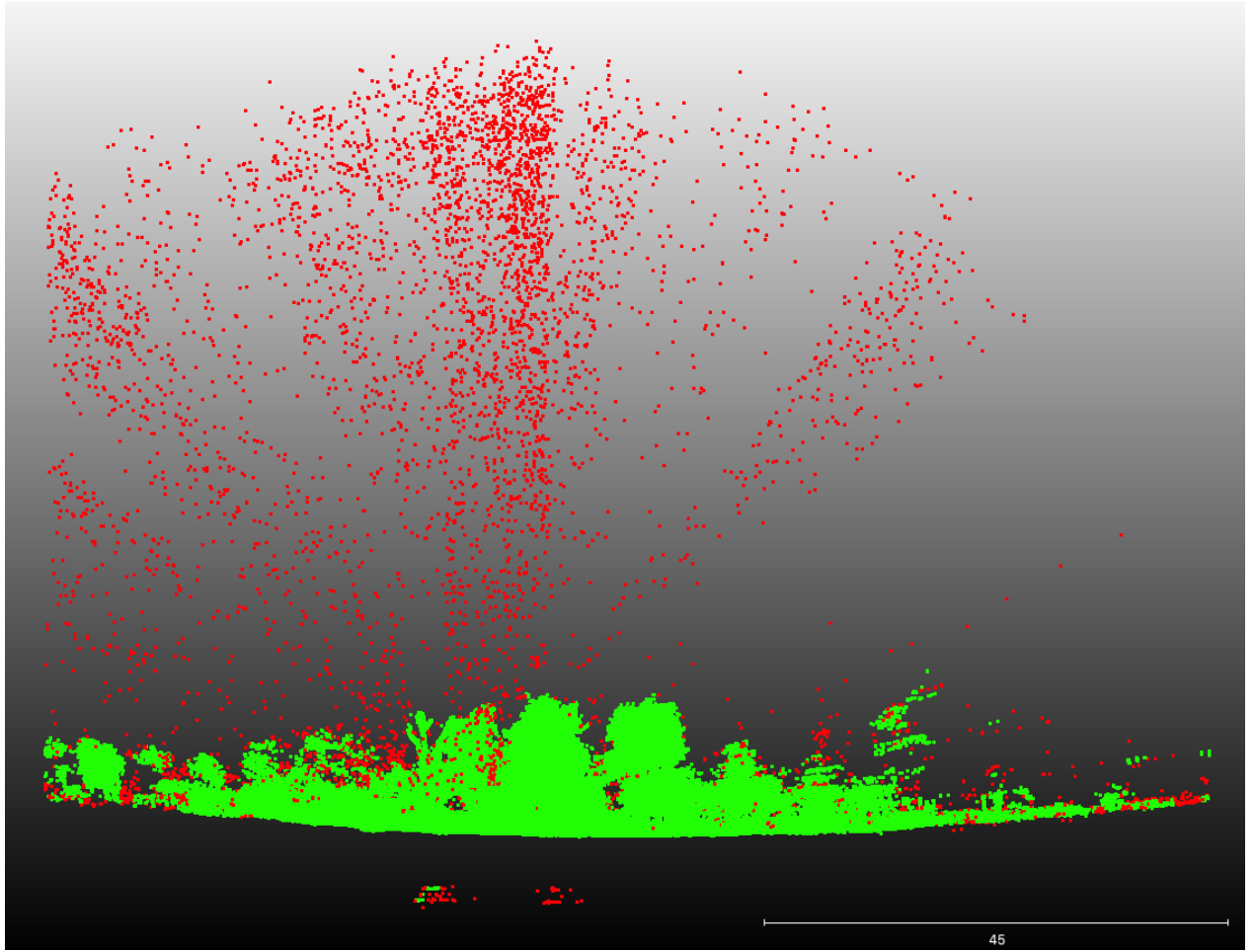


Figure 9: 2 m deep cross section of subplot showing the efficacy of the noise reduction and voxelisation process. Red points are points excluded by this cleaning process, while green points are used in further analysis.

121 4.3 LiDAR analysis

122 4.3.1 Foliage density profiles

123 To estimate subplot foliage density profiles, first the point cloud was cropped to a 10 m diameter cylinder of infinite height. Then the `filters.pmf` (Progressive Morphological Filter - PMF) PDAL function was used to identify ground points (*sensu* Zhang et al. 2003). The `filters.hag_nn` (Nearest Neighbour) PDAL function was used to generate height above ground of each point within the cylinder. Points below ground level were then discarded. Height profile points were exported to a XYZ file then imported into R for further processing.

129 We excluded points above the 99.9th percentile of height, under the assumption that these often
130 constituted noise that had not been adequately removed by PDAL.

131 In R, within each 5 cm width vertical layer, we calculated the foliage density as the proportion of
132 filled 5 cm³ voxels. We filtered the point cloud data to the tree canopy, excluding grass. We identified
133 the breakpoint between the grass understorey and the tree canopy as the first local minima
134 above 1.3 m from the ground.

135 We extracted statistics from the foliage density profile for use in statistical analysis. We first smoothed
136 the density profile using a loess model with a span of 0.1. We then calculated the number of local
137 maxima and minima along the profile. We defined local maxima and minima as points where the
138 foliage density of the surrounding 50 cm of 5 cm bins was lower or higher, respectively.

139 We calculated the effective number of layers (ENL), using the true-numbers equivalent of the Shannon
140 non diversity index (*sensu* (Ehbrecht et al., 2016)). We also calculated the conventional Shannon
141 diversity index on the foliage density of 50 cm bins:

$$H' = - \sum_{i=1}^N p_i \ln p_i \quad (15)$$

142 Where N is the number of 50 cm bins in the height profile, and p_i is the proportion of filled voxels
143 in layer i (foliage density).

144 We calculated the area under the curve of foliage density using trapezoid estimation.

145 We extracted the height of the maximum foliage density peak, and calculated the difference be-
146 tween the highest and lowest local maxima. We also extracted the maximum canopy height within
147 the subplot.

148 We calculated the coefficient of variation of the point cloud height distribution.

149 To describe the uniformity of the foliage density distribution we used Ripley's L function, which is
150 more commonly used in describing spatial variation across a 2 dimensional surface. Ripley's L is

151 an adjustment to Ripley's K, defined as:

$$\widehat{K}(t) = \lambda^{-1} \sum_{i \neq j} \frac{I(d_{ij} < t)}{n} \quad (16)$$

$$\widehat{L}(t) = \left(\frac{\widehat{K}(t)}{\pi} \right)^{1/2} \quad (17)$$

152 We also used the standard error of a linear model of foliage density and height as a simple single
153 number method of describing the uniformity of foliage density. Under a completely even distri-
154 bution of foliage material through the canopy, the standard error should be zero, while clumping
155 causes deviations from this uniform distribution and increases the standard error.

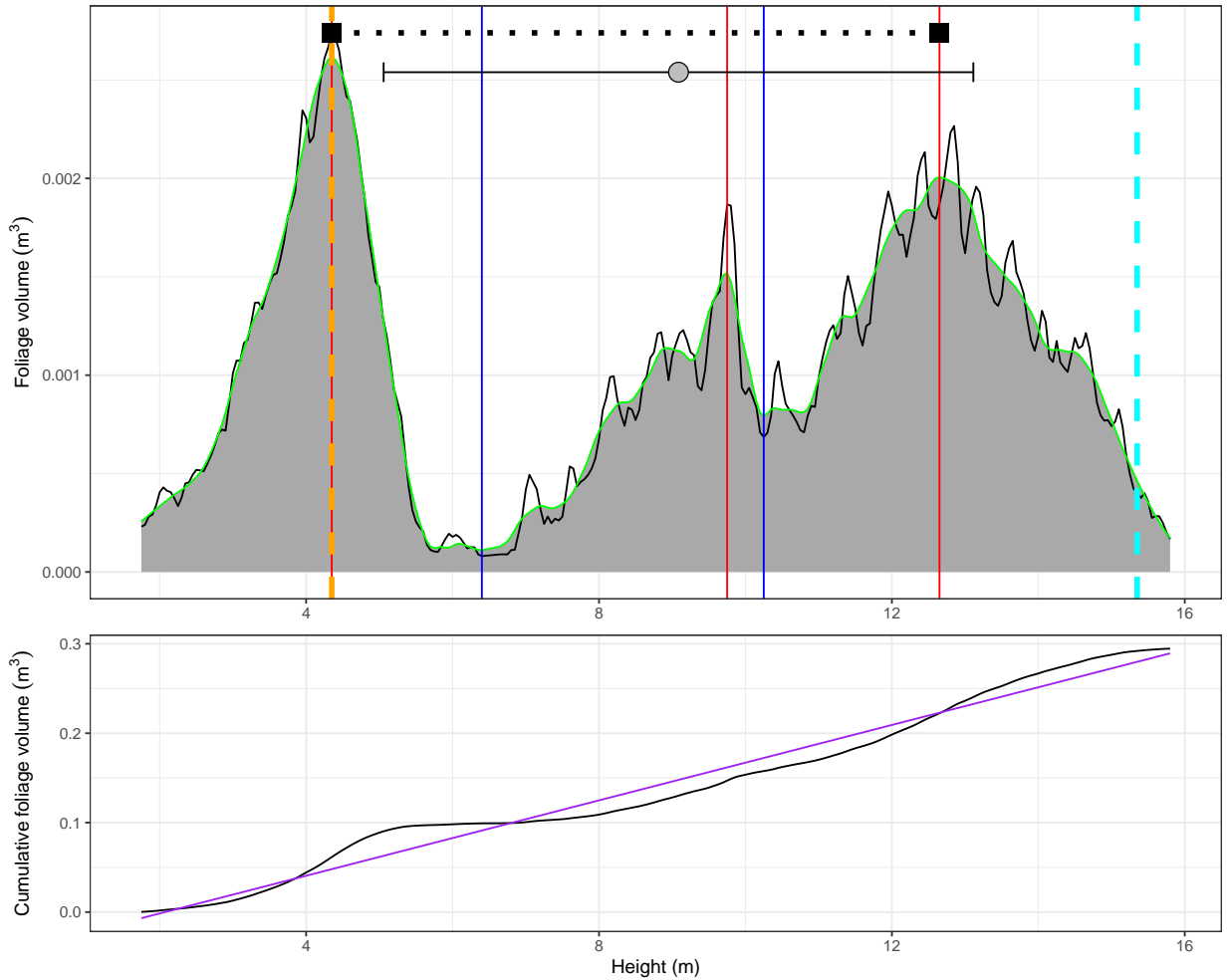


Figure 10: Subplot foliage volume height profile (top) and cumulative foliage volume profile (bottom) for a subplot in Bicuar National Park, to illustrate some of the canopy structure metrics extracted from each height profile. Starting with the top panel: the red lines denote peaks in the distribution, while blue lines represent troughs. The dashed orange line shows the height of the highest peak of foliage density. The dashed cyan line shows the 99th percentile of canopy height, used here as a measure of canopy top height across the subplot. The black squares connected by a dotted line show the layer differentiation, the height difference between the lowest peak and highest peak of foliage density *sensu* Palace et al. (2015). The grey point with interval lines shows the mean foliage volume height ± 1 standard deviation. The black trace shows the foliage density height profile, and the green trace shows the loess model fitted to the data, with the area under the canopy shaded grey. The bottom panel: the black trace shows the cumulative foliage volume through the canopy, taken from the loess fit in the top panel. The purple line shows the line of best fit of a linear model through this data. Not illustrated are the effective number of layers, calculated from the Shannon entropy of foliage volume in 0.5 m height bins.

156 **4.3.2 Canopy cover**

157 Due to terrestrial LiDAR measurement locations being spread over the subplot to avoid occlusion
158 of canopy material, we simulated a scan position at the centre of the subplot using the point cloud
159 data from all scans per subplot. Similar to the processing chain for the foliage density profiles,
160 PDAL was used to crop the point cloud to a 20 m cylinder around the subplot centre, then used
161 `filters.hag_nn` to classify ground points and recalculate height above ground. We cropped the
162 point cloud to points above 1.3 m, with a 50 cm exclusion sphere around the scan position at 1.3
163 m above the ground. The point cloud was converted to a POV-Ray object, where each point was
164 transformed to a 1 cm³ cube. POV-Ray was then used to produce a ray-traced image. As with
165 the hemispherical photos, we used a fisheye lens with an equisolid projection and a view angle of
166 180°, located at the subplot centre, at the same height as the hemispherical photo, with the top
167 of the camera facing magnetic north and the camera facing straight up. Each cube was set as a
168 non-reflective object, and the sky had an equal gamma of 1.0. POV-Ray produced an image of
169 4016x4016 px, identical to the cropped circular dimensions of the images produced by the hemi-
170 spherical photos.

171 Simple canopy cover as seen from the ground was measured using two methods: 1) hemispheri-
172 cal photography and 2) terrestrial LiDAR. Hemiphot () was used to estimate cover from both the
173 hemispherical photos and the TLS POV-Ray simulation. Hemiphot calculates canopy cover in 90
174 evenly sized concentric rings. To obtain the total cover of an image:

$$C_\alpha = 1 - G_{\text{tot}} = \sum_{\alpha=0.5}^{\alpha=89.5} (G_\alpha A_\alpha / A_{\text{tot}}) \quad (18)$$

175 Where G_α is the fraction of unfilled pixels in ring α , A_α is the sky area of the ring segment, and
176 A_{tot} is the total sky area of the hemisphere.

177 We compared canopy cover estimates from both the TLS and hemispherical photo using a linear
178 mixed model which accounted for variation among plots and between the two sites. While plots in
179 Mtarure had a marginally steeper slope, this difference was not significant. We found that hemi-
180 spherical photography almost exclusively under-estimated canopy cover, except in the most open
181 subplots. Additionally, at lower canopy cover the under-estimation of canopy cover by hemispheri-
182 cal photography was larger (Figure 11).

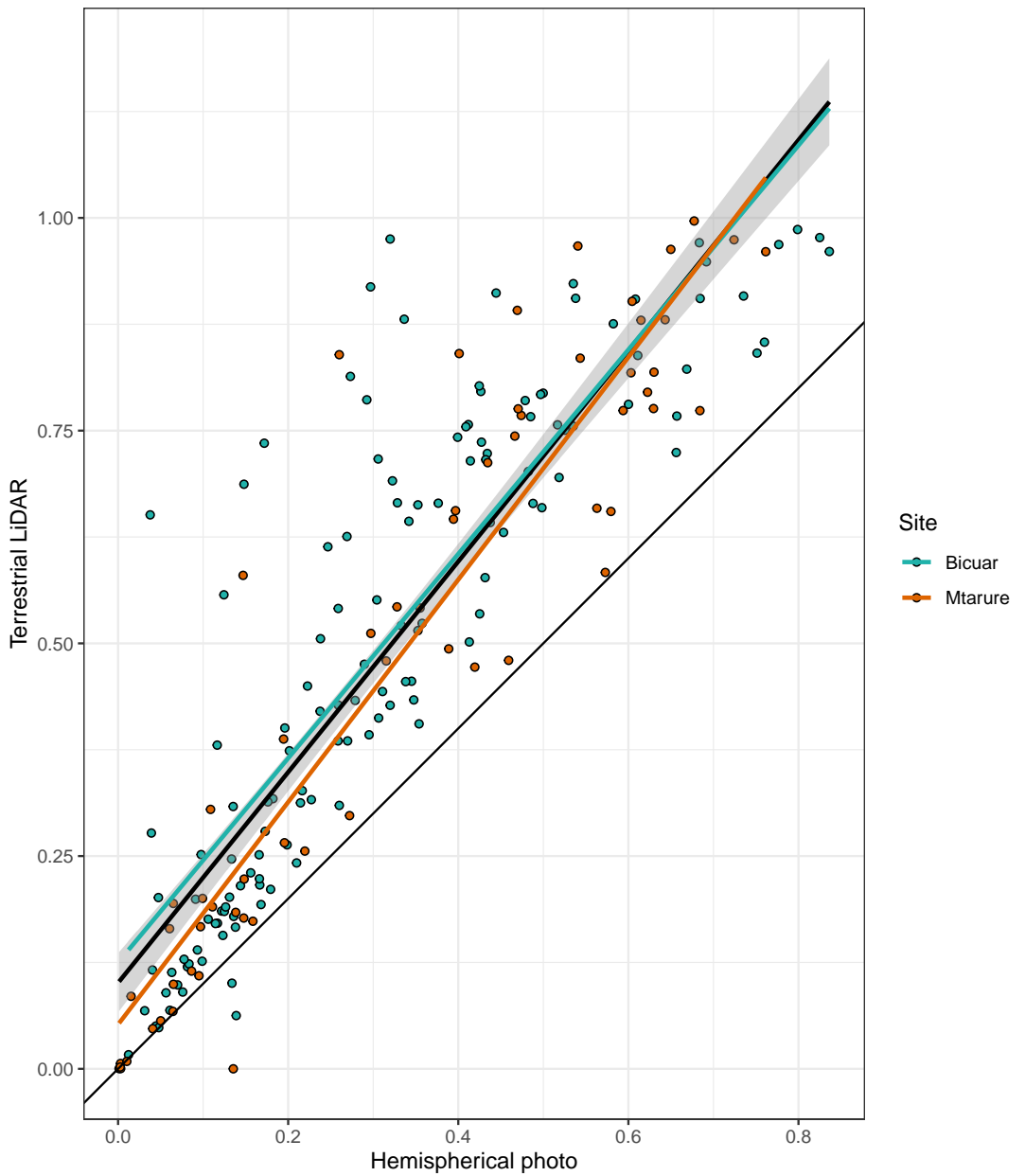


Figure 11: Comparison of canopy cover estimation from TLS and hemispherical photography. The black line of best fit is a linear model of all points ± 1 standard error, while the coloured lines are site specific linear models.



Figure 12: Comparison of hemispherical images for a single subplot in Bicuar National Park. The left image is generated from a hemispherical photo, while the right image is generated from multiple laser scans modelled as cubic voxels with POV-Ray (right).

183 **4.3.3 Grass biomass estimation**

184 An allometric model was developed to estimate grass biomass at every disc-pasture sample point
185 using the grass biomass sample masses. This model was only developed for Angola where grass
186 biomass samples were weighed. The model consisted of a linear mixed effects regression testing
187 the relationship between disc-pasture height (independent) and grass biomass (dependent), with a
188 random slope term for each 1 ha plot.

189 Grass volume was measured from TLS point cloud data following the methodology of. First the
190 point cloud was cropped to points below 2 m. The point cloud was then aggregated to cubic vox-
191 els of 2 cm^3 . Within each vertical 2 cm^2 column, the mean height of points was calculated, then
192 the volume below the mean was assumed to be entirely filled with grass material.

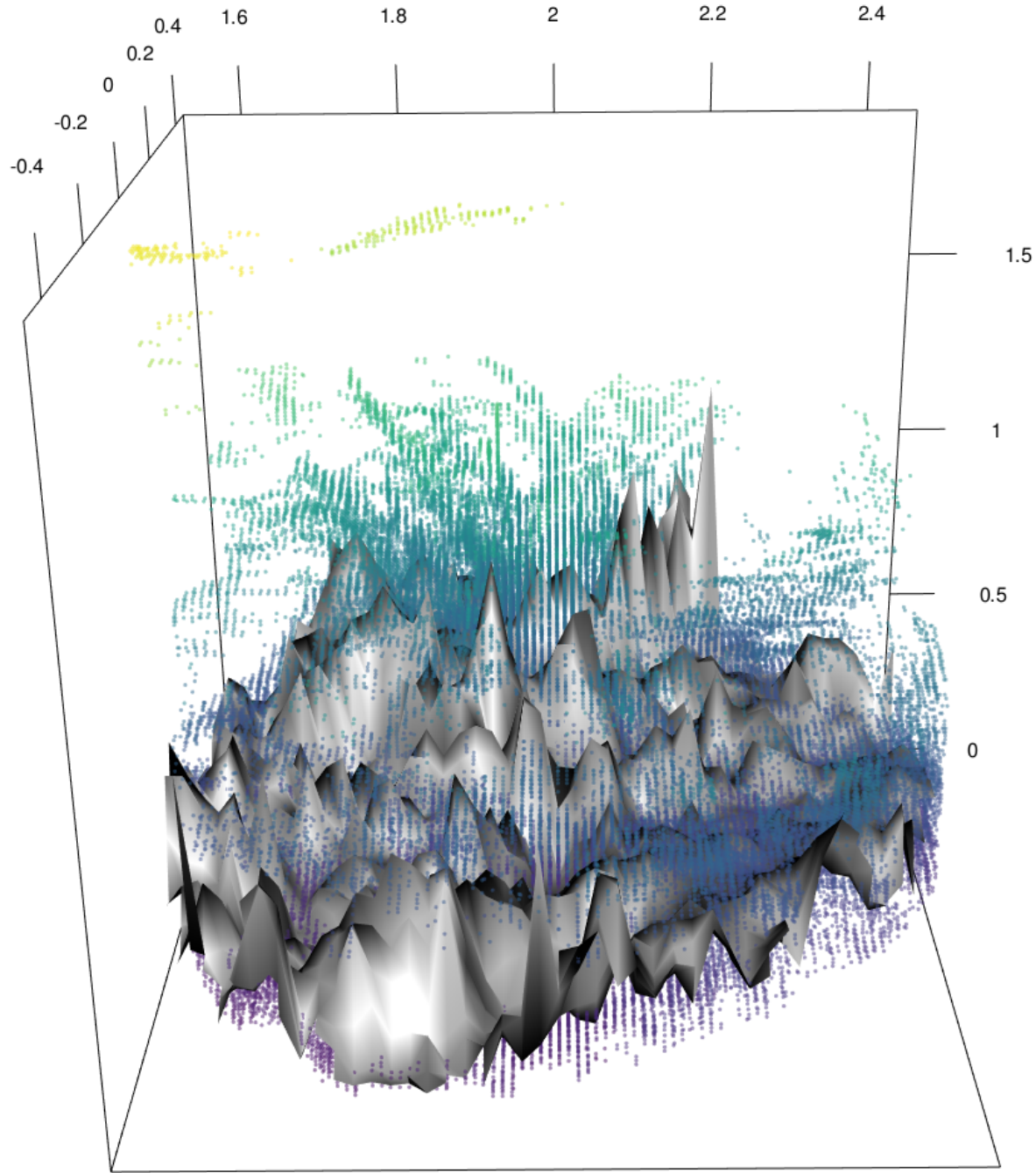


Figure 13: Point cloud with mean heights for each 2 cm^2 column labelled and the estimated grass volume below.

¹⁹³ **4.3.4 Canopy rugosity**

¹⁹⁴ The canopy rugosity of each 1 ha plot was estimated. All scans from each plot were merged to a
¹⁹⁵ single point cloud, and noise reduction was performed as described above and the cloud was vox-
¹⁹⁶ elised to 10 cm^3 cubic voxels. The point cloud was cropped to the plot boundaries, which were
¹⁹⁷ located with dGPS similar to the LiDAR targets.

¹⁹⁸ A canopy height model was produced to describe the upper canopy surface. The 99th percentile of

199 height in each 10 cm^2 vertical column was extracted. The maximum height was not used as this
 200 occasionally constituted a severe outlier which skewed further canopy height model smoothing.
 201 We used the pit-filling algorithm described in Khosravipour et al. (2014) to smooth the canopy
 202 height profile by removing gaps within trees caused by incomplete penetration of the LiDAR beam
 203 (Figure 14).

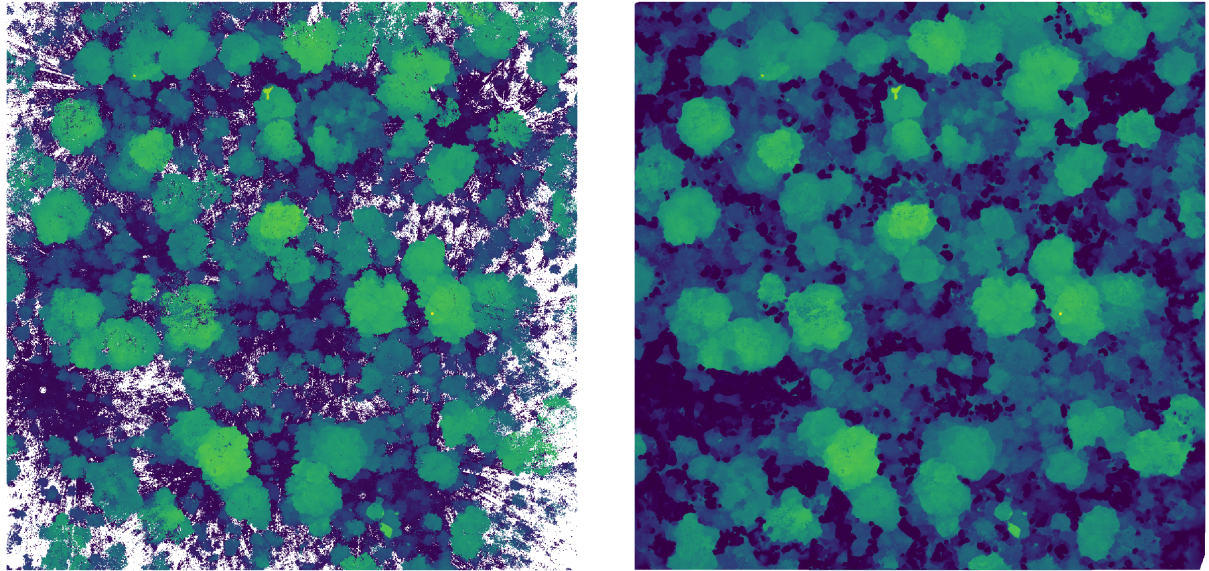


Figure 14: Top-down view of a 1 ha plot in Bicuar National Park. a) shows the point cloud after voxelisation, noise reduction, and taking the 99th percentile of stem height in each 5 cm vertical bin. b) shows the same point cloud after pit filling to generate a smooth canopy height profile. Points are coloured according to point height from the ground.

204 From the canopy height profile we extracted a number of statistics for use in statistical modelling.
 205 We calculated the mean and coefficient of variation of canopy height across the plot (canopy ru-
 206 gosity), following (Parker and Russ, 2004). We calculated the Topographic Ruggedness Index
 207 (TRI) as the mean of absolute differences between the heights of each column and the height of
 208 its eight surrounding cells (Wilson et al., 2007). From this we estimated the plot level mean TRI
 209 and coefficient of variation.
 210 We also calculated a second measure of canopy rugosity (R_c) that considers the entire canopy pro-
 211 file, rather than just the canopy top, following Hardiman et al. (2011)

$$R_c = \sigma(\sigma G_z)_x \quad (19)$$

212 Where G_z is the vertical height axis z , x is the horizontal axis, and σ is the standard deviation.

213 **5 Statistical analysis**

214 All linear mixed effects models were conducted using the `{lmer}` package in R version 4.0.2 (R
215 Core Team, 2020).

216 **5.1 Foliage density profiles**

217 We conducted a number of linear mixed effects models to assess the effects of tree diversity and
218 stand structure on various aspects of canopy structure measured at the 10 m subplot scale. Lin-
219 ear mixed effects models were used to account for the non-independence of samples caused by
220 the nested sampling structure of subplots within plots, and plots within sites. For each subplot
221 canopy structure measure, we created a linear mixed effects model with fixed effects of subplot
222 species richness, and tree spatial structure using the adapted Hegyi index (H_i) and the coefficient
223 of variation of stem diameter. We compared the standardized effect sizes of each fixed effect to
224 understand the relative effect of species richness and spatial structure on canopy structure. We
225 compared models with all combinations of fixed effects to understand which combination of fixed
226 effects best explained variation in each subplot canopy structure measure. We also compared mod-
227 els to a null model including only random effects of plot and site to evaluate whether this ‘best’
228 model explained real variation in canopy structure.

229 **5.2 Grass biomass**

230 To estimate the correlation between grass volume estimated by TLS and grass biomass estimated
231 from the allometry of DPM height and grass biomass samples, we conducted a linear mixed ef-
232 fects model of grass biomass vs. grass volume, with nested random slope terms for each 1 ha plot
233 nested within site.

234 We conducted a linear mixed effects model to assess the effects of canopy structure on grass vol-
235 ume, with random slope terms for each 1 ha plot nested within site. We began with a maximal
236 model which included fixed effects of subplot tree species richness, stem density, TLS canopy cover,
237 layer diversity, height of maximum foliage density, standard deviation of the foliage density pro-
238 file, and our simple measure of foliage density uniformity. We re-fitted the model with all possible
239 combinations of fixed and random effects and compared AIC, BIC, and log-likelihood to determine
240 which combination of explanatory variables best accounted for variation in grass volume. Once
241 this ‘best model’ had been identified we extracted standardized effect sizes for each fixed effect to
242 compare their relative contribution to the model. We also compared random effects for each fixed
243 effect to understand how the relationship differed between the two sites.

244 5.3 Canopy rugosity

245 To understand the effect of species composition and stand structure on whole-plot canopy rugos-
246 ity, we conducted a linear mixed effects model with fixed effects of tree species shannon diver-
247 sity index, stem density, spatial mingling index and winkelmass, with random intercept terms for
248 each site. We extracted slopes for each fixed effect to compare their effect sizes and compared our
249 model with a null model which consisted only of the random effect of site and the fixed effect of
250 stem density.

251 **References**

- 252 Bransby, D.I. and N.M. Tainton (1977). "The disc pasture meter : Possible applications in grazing
253 management". In: *Proceedings of the Annual Congresses of the Grassland Society of Southern
254 Africa* 12.1, pp. 115–118. DOI: 10.1080/00725560.1977.9648818.
- 255 Brusa, A. and D. E. Bunker (2014). "Increasing the precision of canopy closure estimates from
256 hemispherical photography: Blue channel analysis and under-exposure". In: *Agricultural and
257 Forest Meteorology* 195-196, pp. 102–107. DOI: 10.1016/j.agrformet.2014.05.001.
- 258 Chen, X. et al. (Sept. 2011). *Trimble RTX, an innovative new approach for network RTK*. Tech.
259 rep. Portland OR, USA: International Technical Meeting of the Satellite Division of the Insti-
260 tute of Navigation, ION GNSS, pp. 2214–2219.
- 261 Cifuentes, Renato et al. (2014). "Effects of voxel size and sampling setup on the estimation of for-
262 est canopy gap fraction from terrestrial laser scanning data". In: *Agricultural and Forest Meteo-
263 rology* 194, pp. 230–240. DOI: 10.1016/j.agrformet.2014.04.013.
- 264 Ehbrecht, Martin et al. (2016). "Effective number of layers: A new measure for quantifying three-
265 dimensional stand structure based on sampling with terrestrial LiDAR". In: *Forest Ecology and
266 Management* 380, pp. 212–223. DOI: 10.1016/j.foreco.2016.09.003.
- 267 Frazer, Gordon W. et al. (Sept. 2001). "A comparison of digital and film fisheye photography for
268 analysis of forest canopy structure and gap light transmission". In: *Agricultural and Forest Mete-
269 orology* 109.4, pp. 249–263. DOI: 10.1016/s0168-1923(01)00274-x. URL: <https://doi.org/10.1016%2Fs0168-1923%2801%2900274-x>.
- 271 Hardiman, Brady S et al. (2011). "The role of canopy structural complexity in wood net primary
272 production of a maturing northern deciduous forest". In: *Ecology* 92.9, pp. 1818–1827. DOI: 10.
273 1890/10-2192.1.
- 274 Hegyi, F. (1974). "A simulation model for managing jack-pine stands". In: *Royal College of Forestry,
275 editor*. Stockholm, Sweden: Royal College of Forestry, pp. 74–90.

- 276 Hu, Lile and Jiaojun Zhu (May 2009). “Determination of the tridimensional shape of canopy gaps
277 using two hemispherical photographs”. In: *Agricultural and Forest Meteorology* 149.5, pp. 862–
278 872. DOI: 10.1016/j.agrformet.2008.11.008. URL: <https://doi.org/10.1016/j.agrformet.2008.11.008>.
- 280 Hui, G. and M. Albert (2004). “Stichprobensimulationen zur Schätzung nachbarschaftsbezogener
281 Strukturparameter in Waldbeständen [Simulation studies for estimating neighborhood-based
282 structural parameters in forest stands]”. In: *Allgemeine Forst und Jagdzeitung* 175, pp. 10–11.
- 283 Hui, G., K. von Gadow, et al. (2007). *Structure-based forest management*. Beijing, China: China
284 Forestry Publishing House.
- 285 Hui, G., X. Zhao, et al. (2011). “Evaluating tree species spatial diversity based on neighbourhood
286 relationships”. In: *Forest Science* 57.4, pp. 292–300. DOI: <http://dx.doi.org/10.1093/forestscience/57.4.292>.
- 288 Khosravipour, Anahita et al. (2014). “Generating Pit-free Canopy Height Models from Airborne
289 LiDAR”. In: *Photogrammetric Engineering & Remote Sensing* 80.9, pp. 863–872. DOI: 10.14358/
290 pers.80.9.863.
- 291 Palace, Michael W. et al. (2015). “Estimating forest structure in a tropical forest using field mea-
292 surements, a synthetic model and discrete return LiDAR data”. In: *Remote Sensing of Environ-
293 ment* 161, pp. 1–11. DOI: 10.1016/j.rse.2015.01.020.
- 294 Parker, Geoffrey G and Mary E Russ (2004). “The canopy surface and stand development: assess-
295 ing forest canopy structure and complexity with near-surface altimetry”. In: *Forest Ecology and
296 Management* 189.1-3, pp. 307–315. DOI: 10.1016/j.foreco.2003.09.001.
- 297 R Core Team (2020). *R: A Language and Environment for Statistical Computing*. R Foundation
298 for Statistical Computing. Vienna, Austria. URL: <https://www.R-project.org/>.
- 299 Rusu, Radu Bogdan et al. (2008). “Towards 3D Point cloud based object maps for household envi-
300 ronments”. In: *Robotics and Autonomous Systems* 56.11, pp. 927–941. DOI: 10.1016/j.robot.
301 2008.08.005.
- 302 Seidel, Dominik, Stefan Fleck, and Christoph Leuschner (2012). “Analyzing forest canopies with
303 ground-based laser scanning: A comparison with hemispherical photography”. In: *Agricultural
304 and Forest Meteorology* 154–155, pp. 1–8. DOI: 10.1016/j.agrformet.2011.10.006.
- 305 SEOSAW (2020). “A network to understand the changing socio-ecology of the southern African
306 woodlands (SEOSAW): Challenges, benefits, and methods”. In: *PLANTS, PEOPLE, PLANET*.
307 DOI: 10.1002/ppp3.10168.
- 308 von Gadow, K. and G. Hui (2002). *Characterising forest spatial structure and diversity*. Ed. by L.
309 Bjoerk. Lund, Sweden, pp. 20–30.

- 310 Wilson, Margaret F. J. et al. (2007). "Multiscale Terrain Analysis of Multibeam Bathymetry Data
311 for Habitat Mapping on the Continental Slope". In: *Marine Geodesy* 30.1-2, pp. 3–35. DOI: 10.
312 1080/01490410701295962.
- 313 Zhang, Keqi et al. (2003). "A progressive morphological filter for removing nonground measure-
314 ments from airborne LiDAR data". In: *IEEE Transactions on Geoscience and Remote Sensing*
315 41.4, pp. 872–882. DOI: 10.1109/tgrs.2003.810682.